The evolution of a localized vortex disturbance in external shear flows. Part 2. Comparison with experiments in rotating shear flows

By EDWIN MALKIEL, VLADIMIR LEVINSKI
AND JACOB COHEN

Faculty of Aerospace Engineering, Technion – Israel Institute of Technology, Haifa 32000, Israel

The evolution of artificially generated localized disturbances in the shape of hairpin vortices, in laminar axisymmetric rotating shear flows, is investigated experimentally. The results are compared with the predictions of a theoretical model (Levinski & Cohen 1995) with respect to the growth of such disturbances. Hairpin vortices were generated at the surface of the inner cylinder of an axisymmetric Couette apparatus, employing an injection–suction technique. The flow field was analysed from flow visualization using top and side views and by measurements of the mean and instantaneous velocity fields, carried out using laser Doppler anemometry and particle image velocimetry. An instability domain, within the range of base flow parameters where the flow is known to be linearly stable, was found. The marginal ratio between the angular velocities of the inner and outer cylinders beyond which the flow is stable to finite-amplitude localized disturbances agrees with the theoretical prediction based on the measured mean flow in the region of the disturbance. The dependence of the hairpin's inclination angle on the ratio between the two angular velocities is fairly well predicted by the theoretical model.

1. Introduction

In the present paper, the evolution of finite-amplitude localized disturbances in laminar rotating shear flows is investigated experimentally. This is a sequel to the theoretical contribution of Levinski & Cohen (1995, hereinafter referred to as LC). Specifically we study the growth of artificially generated localized disturbances with the shape of hairpin vortices. Side and top views of these vortices, generated in our apparatus, can be seen in figure 4 which will be discussed later.

Prior to the first published observations of hairpin vortices, Theodorsen (1952) suggested such structures, inclined at 45° to the mean flow direction, as a conceptual model for rationalizing momentum transport in turbulent boundary layers. In 1967, Kline *et al.* revealed these well-organized vortex structures in the near-wall region of a turbulent boundary layer. Following this pioneering work, these structures were reported by a growing list of researchers who suggested hairpin type vortices as one of the basic flow structures of turbulent boundary layers. Although other kinds of vortical structures have been reported in the literature (e.g. 'one-legged hairpin': Robinson 1991, 'funnel-shape': Kaftori, Hetsroni & Banerjee 1994), here we shall focus on *symmetrical hairpins*. In order to examine carefully the development of these vortical structures, Acarlar & Smith (1987*a*, *b*) conducted a series of experiments in

which hairpin vortices were artificially generated in a subcritical laminar flat-plate boundary layer. They illustrated that many of the flow patterns generated by the symmetric hairpin vortices in a laminar boundary layer appear markedly similar to fully developed turbulent boundary layer flow patterns. For a detailed review on the subject, the reader is referred to the brief summary of papers given in the article by Head & Bandyopadhyay (1981), and the review articles by Robinson (1991) and by Smith & Walker (1995).

In this paragraph we list the main findings from previous studies which are relevant to the present paper. Hairpin vortices are formed naturally in turbulent boundary layers and may be generated artificially in laminar boundary layers. These vortical structures consist of a pair of counter-rotating 'legs' joined by a relatively short 'head' segment. Hairpin vortices were found to be inclined at 45° to the main flow direction, and remain identifiable even at high Reynolds numbers of the order of $Re_\theta \simeq 10000$ (Head & Bandyopadhyay 1981). In time these vortices grow and extend throughout a substantial part of the boundary layer and beyond it. In laminar boundary layers, it was found that their shape and inclination angle are independent of the method used to excite them (Acarlar & Smith 1987a, b). Because of their dipole structure and their non-wall-normal orientation, the hairpin vortex can function as a pump that transports low-momentum fluid (in between its legs) from the wall to the outer region of the boundary layer.

In order to understand the mechanism leading to the rapid growth of hairpin vortices in boundary layers, LC focused on the evolution of localized disturbances, all dimensions of which are much smaller than the length scale characterizing variations of the basic (unperturbed) fluid-velocity gradient. The velocity field (U_T) is represented by the sum $U_T = U + u$, where U is the base flow field and u is a localized finite-amplitude velocity perturbation. In addition, LC used the fluid impulse integral to characterize the disturbance. Its definition is

$$p = \frac{1}{2} \int r \times \omega(r) \mathrm{d}V, \tag{1}$$

where r is the position vector, $\omega = \nabla \times u$ is the disturbance vorticity vector, $\mathrm{d}V$ is a volume element, and the integration extends over the entire fluid domain.

The fluid impulse is an appropriate characteristic of localized vortex structures since it combines the geometrical dimensions of the structure with the intensity of its vorticity field. Moreover, in unbounded three-dimensional flows, its value is not modified by self-induced motion (Batchelor 1967). Consequently, the evolution of the fluid impulse satisfies a linear equation, even though the fluid motion itself is governed by inherently nonlinear effects. While the integral character of the fluid impulse does not provide the details of flow within the disturbed vortical region, this insensitivity yields, in turn, some universal properties.

Utilizing the compactness of the disturbance, the vorticity equation has been integrated analytically, leading to the evolution equation for the fluid impulse

$$\frac{\mathrm{d}p}{\mathrm{d}t} = -\nabla(p \cdot U) - \tfrac{1}{2}\Omega \times p. \tag{2}$$

The vectors U and Ω are represented here by the leading terms of the respective Taylor-series expansions of the base flow in the vicinity of the moving disturbance.

Analysis of this equation shows that unidirectional planar shear flows are always unstable with respect to finite-amplitude localized disturbances. Furthermore, the analysis predicts that the growing vortex is inclined at 45° relative to the base flow

direction. These predictions agree with existing experimental observations concerning the growth of hairpin vortices in laminar and turbulent boundary layers. Finally, the above vector equation is equivalent to a system of coupled linear equations for the respective streamwise and cross-stream scalar components of the fluid impulse. Analysis of this system suggests a simple feedback mechanism by which one component of the fluid impulse enhances the growth of the other and vice versa. Thus, the dynamics of the localized vorticity disturbance is governed by two mechanisms: one is the lift-up of the disturbance in the cross-stream direction which stretches the basic spanwise vorticity field and thus generates a disturbance-vorticity component in the cross-stream direction; the other mechanism is associated with the stretching and rotation of this disturbance vorticity by the basic shear field. This intensifies the streamwise vorticity component which in turn induces an increased cross-stream velocity, thereby enhancing the lift-up effect and closing the feedback loop.

The purpose of the present work is to validate the predictions of the above mentioned theoretical model. Here we shall focus on axisymmetric rotating shear flow rather than planar unidirectional flows, because according to our previous studies no stability domain exists for finite-amplitude localized disturbances in the latter case. Such a stability domain does exist in rotating flows owing to the additional dynamic effects resulting from rotation. In the following sections we present the instability criterion associated with this type of flow (§ 2) and then we examine it experimentally (§§ 3–5).

2. Application of the theory to axisymmetric rotating shear flows

In cylindrical polar coordinates (r, ϕ, z), the external velocity is assumed to be given by $\boldsymbol{U} = (U_r, U_\phi, U_z) = (0, V(r), 0)$. We subject this base flow to a three-dimensional localized disturbance, positioned at a radial distance $r = r_d$. We use a coordinate system attached to the disturbance and rotating with it, at an angular velocity $\Omega_d = V(r_d)/r_d$. In the rotating frame, the base flow variables are denoted by the tilde. Accordingly, the expressions for the basic velocity and vorticity are

$$\widetilde{\boldsymbol{U}} = (0, V(r) - \Omega_d r, 0) \quad \text{and} \quad \widetilde{\boldsymbol{\Omega}} = (0, 0, \Omega - 2\Omega_d). \tag{3}$$

For this case, the time evolution of the fluid impulse of the disturbance is given by LC

$$\frac{\mathrm{d}\boldsymbol{p}}{\mathrm{d}t} = -\nabla(\boldsymbol{p} \cdot \widetilde{\boldsymbol{U}}) - \tfrac{1}{2}\left(\widetilde{\boldsymbol{\Omega}} + 2\boldsymbol{\Omega}_d\right) \times \boldsymbol{p}, \tag{4}$$

where $\boldsymbol{\Omega}_d = (0, 0, \Omega_d)$ and the base flow variables are evaluated at r_d.

Equivalently, the time evolution of the three components of the fluid impulse (P_r, P_ϕ, P_z) is described by the following set of equations:

$$\frac{\mathrm{d}P_r}{\mathrm{d}t} = -\tfrac{1}{2}P_\phi \left(\frac{\partial V}{\partial r} - 3\frac{V}{r}\right)\bigg|_{r=r_d} \tag{5a}$$

$$\frac{\mathrm{d}P_\phi}{\mathrm{d}t} = -\tfrac{1}{2}P_r \left(\frac{\partial V}{\partial r} + \frac{V}{r}\right)\bigg|_{r=r_d} \tag{5b}$$

$$\frac{\mathrm{d}P_z}{\mathrm{d}t} = 0, \tag{5c}$$

for which the eigenvalues $\{\lambda_i\}_{i=1}^3$ can be found from the characteristic equation

$$\lambda_i \left\{ \lambda_i^2 - \frac{1}{4} \left[\left(\frac{\partial V}{\partial r} - 3\frac{V}{r} \right) \left(\frac{\partial V}{\partial r} + \frac{V}{r} \right) \right] \bigg|_{r=r_d} \right\} = 0. \tag{6}$$

Hence, the flow under investigation is stable with respect to three-dimensional localized disturbances only if the real part of λ_i is not positive, which leads to the following stability criterion:

$$\left[\frac{\partial V}{\partial r} - 3\frac{V}{r} \right] \left[\frac{\partial V}{\partial r} + \frac{V}{r} \right] \bigg|_{r=r_d} \leqslant 0. \tag{7}$$

It should be noted that according to the Rayleigh criterion for stability, only the sum of the terms in the second brackets of (7) must be positive.

The general solution of (5) is

$$P_r = \tfrac{1}{2} \left(P_r(0) - \beta P_\phi(0) \right) e^{\lambda t} + \tfrac{1}{2} \left(P_r(0) + \beta P_\phi(0) \right) e^{-\lambda t}, \tag{8a}$$

$$P_\phi = -\frac{1}{2} \left(\frac{P_r(0)}{\beta} - P_\phi(0) \right) e^{\lambda t} + \frac{1}{2} \left(\frac{P_r(0)}{\beta} + P_\phi(0) \right) e^{-\lambda t}, \tag{8b}$$

$$P_z = P_z(0), \tag{8c}$$

where $P_r(0)$, $P_\phi(0)$ and $P_z(0)$ are the initial fluid impulse components at $t = 0$ and

$$\lambda = \frac{1}{2} \left(\left(\frac{\partial V}{\partial r} - 3\frac{V}{r} \right) \left(\frac{\partial V}{\partial r} + \frac{V}{r} \right) \bigg|_{r=r_d} \right)^{1/2},$$

$$\beta = \left(\left(\frac{\partial V}{\partial r} - 3\frac{V}{r} \right) \bigg|_{r=r_d} \bigg/ \left(\frac{\partial V}{\partial r} + \frac{V}{r} \right) \bigg|_{r=r_d} \right)^{1/2}. \tag{9}$$

For times much greater than $1/\lambda$, the exponentially growing terms in (8) become dominant and consequently the solution for the fluid impulse can be approximated as

$$P_r = -\beta P_\phi, \tag{10}$$

independent of the initial value of the fluid impulse.

Since the fluid impulse vector is perpendicular to the plane of any vortex dipole such as the hairpin one, the latter is predicted to be inclined to the radial direction at an angle Θ, which is determined by

$$\Theta = \arctan \left(-\frac{P_r}{P_\phi} \right) = \arctan(\beta). \tag{11}$$

Thus, unlike plane shear flows in which the inclination angle of the hairpin vortex is predicted to be 45° (LC), this angle in the case of rotating shear flows is found to be a function of the base flow parameters and the position of the disturbance.

In the following sections, the predictions of the stability criterion (7) and the inclination angle of the vortex disturbance (11) are examined experimentally.

3. Selection of parameters

In order to verify experimentally the theoretical predictions, the stability of Couette flow between two concentrically rotating cylinders with respect to localized disturbances is investigated.
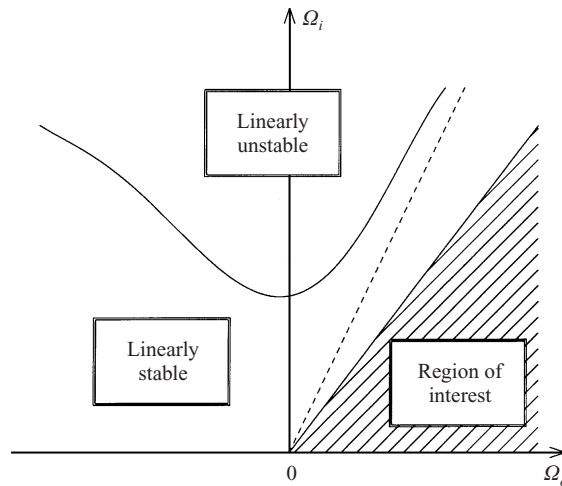
FIGURE 1. Stability diagram for axisymmetric Couette flow. The dashed line corresponds to Rayleigh's criterion. The solid line corresponds to the curve of marginal stability of the flow with respect to small-amplitude viscous disturbances. The upper boundary of the shaded area is given by (17).

3.1. *Base flow parameters*

For axisymmetric Couette flow, the azimuthal component of the basic velocity is given by (Koschmieder 1993, p. 211)

$$V(r) = \frac{\Omega_o R_o^2 - \Omega_i R_i^2}{R_o^2 - R_i^2} r + \frac{(\Omega_i - \Omega_o) R_o^2 R_i^2}{R_o^2 - R_i^2} \frac{1}{r}, \tag{12}$$

where R_i and R_o are the radii of the inner and outer cylinders, respectively, and Ω_i and Ω_o denote the angular velocity of rotation about the common axis of the two cylinders.

The stability criterion in this case is obtained by substituting (12) into (7):

$$(\Omega_o R_o^2 - \Omega_i R_i^2) \left[(\Omega_o R_o^2 - \Omega_i R_i^2) + \frac{2(\Omega_i - \Omega_o) R_o^2 R_i^2}{r_d^2} \right] \geqslant 0. \tag{13}$$

In his experimental work, Coles (1965) distinguished the region of parameters in which the flow is dominated by rotation of the outer cylinder from the region where the flow is dominated by rotation of the inner cylinder. In the latter case, he reported that transition to turbulence occurred through the process of slow spectral evolution associated with Taylor instability, whereas for flows dominated by the rotation of the outer cylinder, transition occurred only when sufficiently strong disturbances were present. Here we shall concentrate on this case and to ensure that Taylor instability is avoided we choose the parameters so that the flow is stable according to the Rayleigh inviscid criterion.

The Rayleigh criterion predicts the flow to be stable only if both cylinders rotate in the same direction and

$$\Omega_o R_o^2 > \Omega_i R_i^2. \tag{14}$$

The criterion is shown schematically in figure 1 by the dashed line, where the region of stability is to the right of it. In the figure we also include the curve of marginal stability (solid line) of viscous Couette flow with respect to all kinds of small-amplitude disturbances.

To the right of Rayleigh's criterion (our region of interest), the sum of terms within the first parenthesis of (13) is positive and therefore the criterion for stability (13) is reduced to

$$\Omega_o R_o^2 (2R_i^2 - r_d^2) \leqslant \Omega_i R_i^2 (2R_o^2 - r_d^2). \tag{15}$$

Provided the initial position of the localized disturbance $r_d \geqslant \sqrt{2}\, R_i$, the above expression (15) is satisfied and the flow is stable in this region. However for $r_d < \sqrt{2} R_i$, the flow becomes unstable if

$$\Omega_i < \Omega_o \frac{R_o^2}{R_i^2} \frac{2R_i^2 - r_d^2}{2R_o^2 - r_d^2} \tag{16}$$

and relation (14) holds.

When $r_d = R_i$, the instability criterion is

$$\Omega_i / \Omega_o < R_o^2 / (2R_o^2 - R_i^2). \tag{17}$$

Thus, as the angular velocity of the inner cylinder is decreased below this value, instability, which first occurs in the region adjacent to the inner cylinder, begins. The shaded area in figure 1 corresponds to the region where we anticipate the flow to be unstable with respect to finite-amplitude localized disturbances. The upper boundary of this area is given by (17). The experiments reported in the following are focused on this regime of the base flow parameters.

3.2. *Disturbance flow parameters*

In order to estimate the size of the initial disturbance, one has to take into account the effect of viscosity. As was shown by LC, the formal inclusion of the viscous term in the vorticity equation does not contribute to the dynamics of the fluid impulse associated with the localized disturbance. However, viscosity plays a crucial role in the generation of the initial localized disturbance. To estimate this effect we consider the structure of horseshoe or hairpin vortices in relation to the theoretical assumption (LC) that the concentrated disturbed vorticity is confined to a small region.

Based on flow visualization experiments, this vortical structure consists of a pair of counter-rotating legs, joined by a relatively short 'head' segment. For such dipole vortical configurations, the cross-section radius of each leg (r_c) must be smaller than the distance between the centres of the two legs (d). Otherwise, viscous diffusion can lead to vorticity cancellation and to the elimination of the vortex.

In equilibrium, the thickness of each leg can be obtained from the balance of two opposite processes: the cross-section expansion of each leg due to viscous diffusion and its reduction due to the stretching of the vortex. The expansion due to viscous diffusion can be estimated from the solution of the diffusion equation, i.e. $r_c^2 \sim 4vt$, where v is the kinematic viscosity. Thus, the rate at which the cross-section radius of each leg is increased is given by

$$\left(\frac{\mathrm{d}r_c}{\mathrm{d}t} \right)_{dif} \sim 2\frac{v}{r_c}. \tag{18}$$

On the other hand, the long-time behaviour of (5) implies that

$$\frac{\mathrm{d}|\boldsymbol{p}|}{\mathrm{d}t} \sim \lambda |\boldsymbol{p}|. \tag{19}$$

As a first approximation we assume that the main contribution to the time variation of the fluid impulse is due to the stretching of the hairpin vortex along its axis. Thus,

(19) can be replaced by $dl/dt \sim \lambda l$, where l is the length of the vortex. Furthermore, assuming that during the stretching of the vortex, the volume of its legs ($\sim lr_c^2$) remains constant, we obtain

$$\left(\frac{dr_c}{dt}\right)_{str} \sim -\tfrac{1}{2}\lambda r_c. \tag{20}$$

The resulting approximation for the equilibrium cross-section radius is obtained by equating (18) with (20)

$$r_c^2 \sim \frac{4v}{\lambda}. \tag{21}$$

For a two-dimensional plane shear layer, for which $\lambda = 0.5 \, dU/dy$ (LC), the equilibrium cross-section radius becomes $r_c \sim 2.8(v/(dU/dy))^{1/2}$. Acarlar & Smith (1987$a, b$) measured the average vorticity within the core of each leg and its associated circulation (Γ). They reported that $\omega/(dU/dy) = 0.88 \pm 0.12$ and $\Gamma/v = 65 \pm 30$. Thus, the resulting average value of the measured core radius is $r_c = (\Gamma/(\pi\omega))^{1/2} = 4.8(v/(dU/dy))^{1/2}$. This relationship is similar to the one suggested by the above approximation. Furthermore, the crude estimation of the core radius agrees with the lower limit found by Acarlar & Smith (1987a, b) and is 1.7 times smaller than the averaged measured value.

As was mentioned above, the distance between the two legs (d) must be larger than the core size of each leg. Therefore, for axisymmetric Couette flow, for which the inner cylinder is assumed to be stationary and the disturbance is positioned at R_i, our estimation (21) gives

$$d \geqslant 2\left(\frac{v}{\lambda}\right)^{1/2} = 2\left(\frac{v(R_o^2 - R_i^2)}{\Omega_o R_o^2}\right)^{1/2}. \tag{22}$$

The artificially generated disturbance is positioned at R_i, since according to the theoretical prediction, instability first occurs in the region adjacent to the inner cylinder.

The characteristic upper value of the outer angular velocity is about 60 r.p.m. This leads to a minimal size of the disturbance (in water) of $d_{min} \sim ((R_o - R_i)/R_o)^{1/2}$ mm. Although only local effects are investigated, and for this reason any gap size $R_o - R_i$, could be selected, we decided to use a narrow-gap apparatus to ensure the two-dimensionality of the basic (mean) field. Accordingly, the gap size, the radius of the inner cylinder and the height of the apparatus were chosen to be 0.9, 5 and 24 cm, respectively, which by the use of (22) leads to $d_{min} \sim 0.5$ mm. Therefore, to avoid the effect of viscous diffusion and to ensure that the characteristic scale of the disturbance is much smaller than the spatial scale of the base flow, the size of the disturbance must be about 1–3 mm.

4. Experimental setup

4.1. *Apparatus and measurement techniques*

An axisymmetric Couette apparatus consisting of two concentrically rotating cylinders was built, using water as a working fluid. Hairpin vortices were generated at the inner cylinder by applying suction through two small holes, positioned along the cylinder's axis, and by injecting fluorescent dye through an additional hole located in between. Top- and side-view pictures of the flow were taken with CCD cameras. Measurements
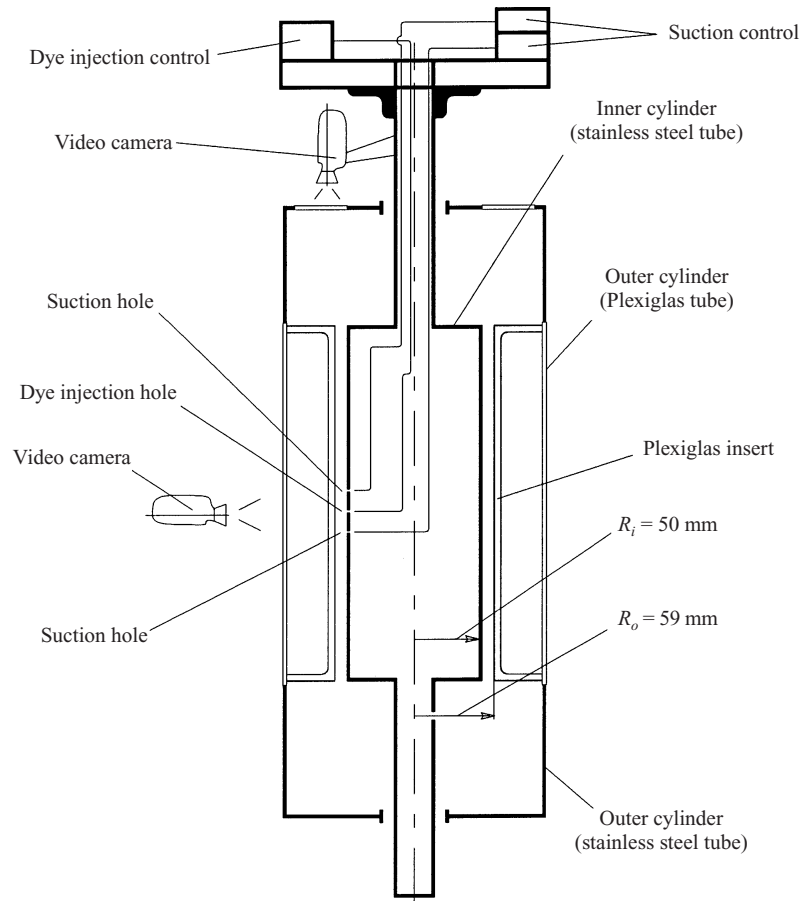
FIGURE 2. Schematic cross-sectional side view of the Couette apparatus.

of the mean and instantaneous velocity fields were carried out using LDA (laser Doppler anemometry) and PIV (particle image velocimetry) techniques.

A schematic cross-sectional side view of the Couette experiment is shown in figure 2. The apparatus was designed to rotate two coaxial (inner and outer) cylinders independently. Each cylinder was supported by ball bearings on each side and driven from below. They were connected to DC motors via belts and worm gears. The angular velocities of the cylinders were controlled by regulating the voltage to the motors. For the present investigation, the outer rotation was varied between 20 and 70 r.p.m., while the inner ran from 0 to 50 r.p.m. Their velocities were monitored during experiments and typically varied less than 0.2% for the duration of measurements.

The apparatus was designed for two geometrical configurations, that with a wide gap and that with a narrow gap between the two cylinders. The inner cylinder of the apparatus had an outside diameter of 100 ± 0.1 mm while the outer cylinder had an inside diameter of 190 ± 0.1 mm leaving a gap of 45 mm between them. The length of this gap was 430 mm, giving a meridional cross-section with an aspect ratio of about 10. The narrow-gap configuration, whose purpose was to minimize end effects, included a Plexiglas insert with an inside diameter of 118 ± 0.1 mm and a length of 240 mm, which reduced the gap to 9 mm and made the aspect ratio 27. The top and bottom ends of the narrow gap were also separated a significant distance from the

corresponding endwalls, which rotate with the outer cylinder and thus do not make suitable end conditions for the theoretical profile (12).

The apparatus was specifically designed to allow top and side views of hairpins for flow visualization from an observing video camera which could rotate with the inner cylinder. For flow visualization purposes, the hairpins were coloured with a fluorescent dye (a mixture of flourescein and alcohol that had a specific gravity of 1) and illuminated from the side by focusing UV light from black light lamps through the transparent middle section of the outside cylinder. In addition, a non-rotating triggerable CCD camera was used to capture digital images of the dyed hairpins when illuminated by a laser light sheet, as discussed below.

The azimuthal velocity in the gap was measured with a backscattering dual beam LDA fibre optic system purchased from Dantec and processed using their Burst Spectrum Analyzer. The LDA experiments were conducted in water uniformly seeded with 2 and 4 micron Polystyrene spheres. Because their specific gravity is close to that of water, they could remain suspended during a full set of LDA measurements which could take several hours. The LDA system was used with a 5 W argon ion laser operating at 2 W. The beam was split, frequency shifted for directional measurement, passed through a beam expander and focused through a 600 mm focal length lens. The two resulting beams converged through a Plexiglas window attached to the top end of the outer cylinder and intersected each other to define an ellipsoidal probe volume with its major axis parallel to the axes of the cylinders. The length of the major axis was 3.2 mm while the diameter of the probe volume was 0.15 mm. The positioning of this volume would vary ± 0.1 mm in the radial direction due to optical non-uniformity of the window. Because the probe location would oscillate as the outer cylinder (and attached window) rotated, exact integer ratios between the outer and inner cylinder rotation rates were avoided. Over long sampling times, this eliminated an unwanted link between the probe's angular position relative to the suction holes on the inner cylinder and its radial location, and made it such that the data were effectively averaged over $\Delta r \leqslant 0.35$ mm.

LDA velocity data for the bulk of the work presented was phase-locked with respect to the angular position of the suction holes on the inner cylinder. With the help of a reference trigger signal, the occurrence times of Doppler bursts (velocity data) were converted to map the corresponding angular distances of the probe volume (data locations) from the suction holes on the inner cylinder.

Particle image velocimetry (PIV) was implemented to demonstrate the nature of the flow induced by hairpins in rotating flows. For this purpose, a laser light sheet was passed through the Plexiglas side of the outer cylinder illuminating the midplane of the cylinders which cuts between the two suction holes (and bisects hairpins at their heads). The light sheet was produced by deflecting a shuttered argon ion laser beam on a rotating polygon mirror (whose speed was computer controlled) and subsequently passing the beam through a cylindrical lens so that it would trace a rectilinear sweep over just the region of interest. The sweeping beam was shuttered so that only a pair of consecutive high-intensity sweeps would be produced for the duration of two video frames, even though there would be many more sweeps in that time interval when the mirror would rotate at high speed. The illuminated plane was imaged from above on a double frame cross-correlation CCD camera. Each pair of high-intensity sweeps exposed two individual frames which were subsequently processed with a cross-correlation algorithm to produce vector maps of the flow field. A setup similar to what is described above, but with the light sheet thickness increased to 7 mm (illuminating whole hairpins including their legs), rather than 0.5 mm, was
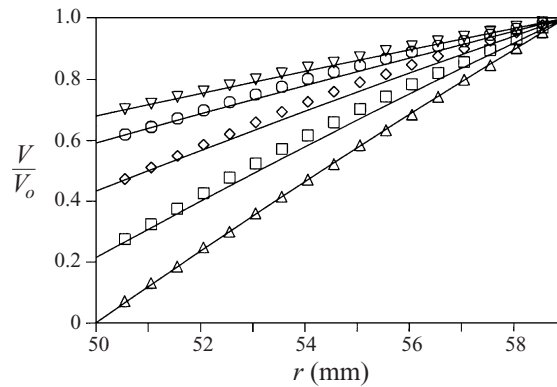
FIGURE 3. Profiles of the mean azimuthal velocity measured at $z = 0$ mm when $\Omega_o = 30$ r.p.m. $\triangle$, $\Omega_i/\Omega_o = 0$; $\square$, $\Omega_i/\Omega_o = 0.25$; $\diamondsuit$, $\Omega_i/\Omega_o = 0.51$; $\bigcirc$, $\Omega_i/\Omega_o = 0.7$; $\triangledown$, $\Omega_i/\Omega_o = 0.8$.

used for capturing digital images of dyed hairpins for the purpose of measuring their angles of inclination.

The PIV experiments utilized 10–20 micron silver-coated hollow glass spheres which on average are slightly heavier than water and have a density which increases with particle diameter. To obtain meaningful velocity measurements on the spatial scale of the hairpin, a seeding concentration of about 4 particles per 1 mm^3 was used. Since water seeded (if the particles are uniformly distributed) to such a degree would scatter the light too much on the 215 mm path from laser sheet to camera, measurements were taken when a significant portion of the particle population had settled, leaving the upper layers of the apparatus relatively free from scattering particles.

4.2. *Mean velocity field*

To check the quality of the apparatus, mean profiles of the azimuthal velocity component $V(r)$ were obtained for various ratios of Ω_i/Ω_o and compared with the theoretical solution (12). The velocity profiles, normalized by the velocity of the outer cylinder V_o, are shown in figure 3 for the case in which $\Omega_o = 30$ r.p.m. The symbols represent the measured data points while the solid lines are the corresponding theoretical profiles. In general, the agreement is fairly good, in particular when the inner cylinder is stationary ($\Omega_i/\Omega_o = 0$) and close to the solid-body rotation limit ($\Omega_i/\Omega_o = 1$). In between these two limits there is a slight deviation of the measured points from the theoretical curve. Similar results were obtained for higher values of Ω_o where this deviation becomes more pronounced. The deviation between the measured velocity and the axisymmetric Couette solution is due to end effects. Such a deviation (although very small: about 2–3%) is still present even for experiments carried out with an apparatus having an extremely large aspect ratio of 233, an order of magnitude larger than that used in our apparatus (Escudier, Gouldson & Jones 1996).

Comparing mean velocity profiles measured over a spanwise distance of ± 15 mm (an order of magnitude larger than the typical size of the disturbance), shows that the mean velocity field is essentially two-dimensional. In addition, all profiles increase monotonically with the radial distance and therefore are stable according to Rayleigh's criterion. These characteristics of the measured mean velocity field are consistent with the flow conditions assumed in §§ 2 and 3.
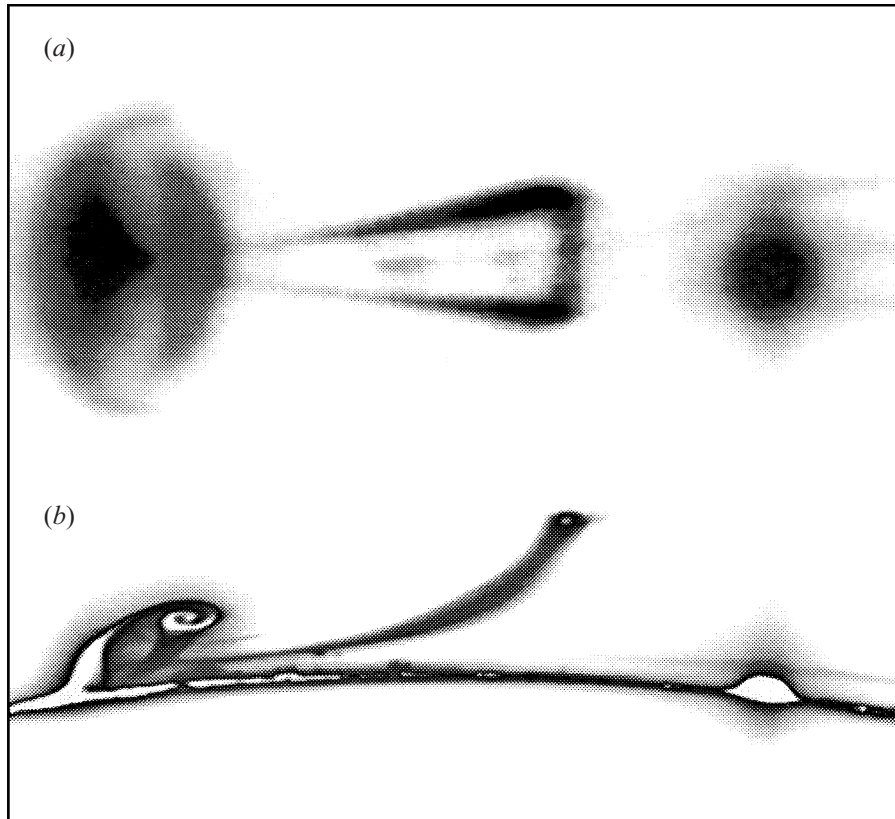
FIGURE 4. Side (*a*) and top (*b*) views of a hairpin in axisymmetric Couette flow when the inner cylinder is stationary and $\Omega_o = 40$ r.p.m. The suction level is 1.47 ml s^{-1}. The outer surface of the inner cylinder is indicated by the black arc in (*b*). The region of generation is on the left and a marker on the surface of the inner cylinder at $\phi = 15°$ appears to the right.

4.3. *Generation of the disturbance*

In order to generate hairpin vortices, we use an injection–suction technique. For this purpose, a horizontal plate was mounted on the top end of the inner cylinder's shaft so that it would rotate with the inner cylinder (see figure 2). This plate served as a stand for a dye injection unit and a displacement type suction pump which were placed on it. The injection unit consisted of a 2l reservoir filled with dilute dye. The dye was injected perpendicularly to the inner cylinder wall through a small hole of diameter 0.5 mm. The dye ran from the reservoir to this hole through a capillary tube under the influence of gravity. The rate of the dye flow was controlled by a valve and monitored by a flow meter mounted on the horizontal plate. Two additional small holes of 1.5 mm in diameter were located 3.5 mm above and below the dye injection hole (in the direction of the cylinder's axis) on the inner cylinder. These holes served for the suction of water around the injection area. The holes were connected through two tubes which ran inside the inner cylinder to the pump unit. The unit consisted of separate pump heads for each line, but mounted on the same shaft of a DC motor. In this way, the amount of flow through each suction hole could be balanced by adjusting the stroke displacement volume of a pump head, while the

overall amount of suction applied was varied by controlling the voltage to the motor. The water that the pump removed was fed back to the system at the lower end of the apparatus.

Hairpins were generated by applying continuous suction to the two holes on either side of the injection hole and by the rotation of the inner and outer cylinders. The values of suction given in this paper refer to the net flow rate through these two holes combined. For a given injection rate and set rotation speeds, a high enough suction level could be applied to keep the flow steady and cause the injected dye to flow in a small and enclosed region adjacent to the wall. Operating at reduced levels of suction caused the expansion of the coloured region and the initiation of periodic shedding of hairpin vortices. The basic structure of a typical growing hairpin vortex is seen in figure 4 where a simultaneously recorded side and top view is presented. It was generated under the conditions of $\Omega_i = 0$, $\Omega_o = 40$ r.p.m., suction at 1.47 $\mathrm{ml\,s^{-1}}$ and with the injection of a dilute flourescein dye at 1.4 $\mathrm{ml\,min^{-1}}$. The flow is from left to right, so the region of generation is on the left and the hairpin is in the centre. The spot to the right is a marker indicating an azimuthal angle of $15°$ from the suction location. (The image of the marker appears much larger than its actual size because of the intensity of the light reflected from it.) The width of the hairpin, which measures about 2 mm, is roughly equivalent to the size of the straight portion at the head of the hairpin in the lower view. As can be seen from the side view, the legs form a roughly triangular shape, probably due to the influence of the upstream hairpin.

The velocity field in the (r, ϕ)-midplane lying between the two legs and bisecting a hairpin at its head, is shown in figure 5. The measurements were obtained by PIV under the conditions of $\Omega_i = 0$, $\Omega_o = 23$ r.p.m. and suction at 1.47 $\mathrm{ml\,s^{-1}}$ (no injection was applied). The vector map (V_ϕ, V_r) of total velocity is shown in figure 5(a), while the map associated with the disturbance field, obtained by subtracting the unperturbed shear flow, is depicted in figure 5(b). The azimuthal location of the suction holes on the inner cylinder (indicated by the solid curve) is marked s. As observed in figure 5(a), downstream of the suction holes, the fluid surrounding the hairpin is ejected outwards, in the radial direction away from the inner cylinder. This ejection, which resembles the bursting phenomenon observed in turbulent boundary layers, is in fact a superposition of the unperturbed flow and the flow induced by the hairpin (figure 5b). The latter consists of an upstream and outward induced velocity between the legs and a vortex flow around its head. As the hairpin travels downstream along the azimuthal direction (figure 5c) it grows (the induced velocity field between its legs occupies a larger region) and moves away from the wall (note the difference in the radial scales between figures 5b and 5c).

In order to examine the influence of injection rates on the generation of hairpin vortices, the boundary indicating to what level the suction had to be reduced for the initial appearance of hairpins was measured for different dye injection rates. Shown in figure 6 are three cases for which the inner cylinder was kept stationary while the outer cylinder was rotated at $\Omega_o = 20$, 40 and 60 r.p.m., and one case for which $\Omega_o = 40$ r.p.m. and $\Omega_i/\Omega_o = 0.27$. As can be seen, for a given Ω_o, there is a range of injection rates for which the suction level corresponding to the first observation of hairpin vortices is approximately constant. We chose to work within this range and selected the injection rate to be 1.2 $\mathrm{ml\,min^{-1}}$ for all cases. The purpose of the suction was to form a small, locally separated region attached to the inner cylinder which caused the generation of the initial vortex disturbance. In that respect, the purpose of the injection was mainly to mark the vortical disturbance. In fact, the
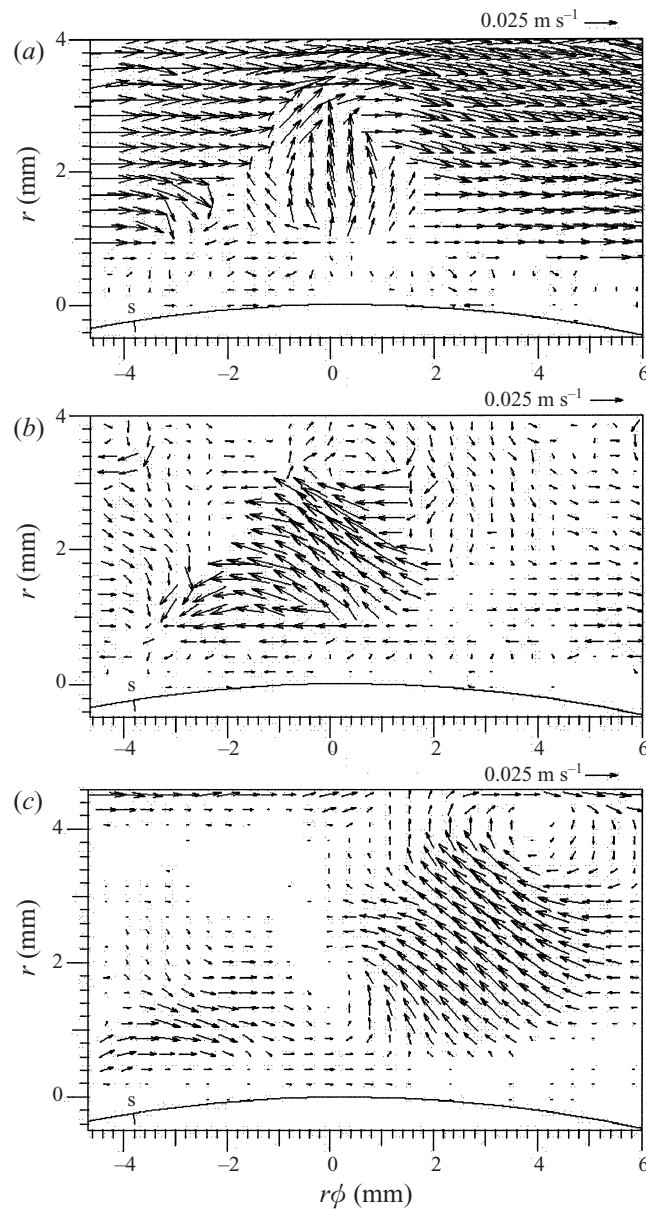
FIGURE 5. The velocity field, obtained by PIV, in the (r, ϕ)-midplane lying between the two legs and bisecting the hairpins at their heads. The inner cylinder is stationary, $\Omega_o = 23$ r.p.m. and the suction level is 1.47 ml s^{-1}. (a) The vector map (V_ϕ, V_r) of total velocity, (b) the vector map associated with the disturbance field, (c) same as (b) but at a later time.

difference between the volumetric suction and injection flow rates was two orders of magnitude. Moreover, using the PIV setup to visualize the situation when no injection was applied, the first appearance of hairpin vortices for the case of $\Omega_o = 40$ r.p.m. occurred at almost the same suction level as for the case with a small amount of injection. This measurement is indicated in figure 6 by the full circle.
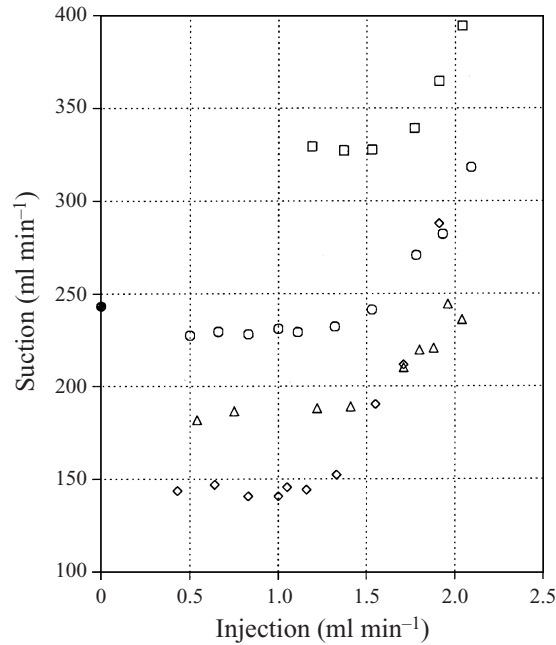
FIGURE 6. Variation of the suction levels, corresponding to the first observation of hairpin vortices, as function of the dye injection rate. $\Diamond$, $\Omega_o = 20$ r.p.m., $\Omega_i/\Omega_o = 0$; $\bigcirc$, $\bullet$, $\Omega_o = 40$ r.p.m., $\Omega_i/\Omega_o = 0$; $\square$, $\Omega_o = 60$ r.p.m., $\Omega_i/\Omega_o = 0$; $\triangle$, $\Omega_o = 40$ r.p.m., $\Omega_i/\Omega_o = 0.27$.

5. Results

In this section we present results of a series of experiments carried out in order to carefully examine the predictions of the model described in §2.

5.1. *The instability domain*

First we establish the range of parameters associated with the local mean flow over which hairpin vortices are observed. For given R_o and R_i, the local mean flow is determined by the angular velocities of the inner and outer cylinders and the level of suction applied.

The domain of instability is shown in figure 7 for the case in which $\Omega_o = 40$ r.p.m. For a given ratio Ω_i/Ω_o, the suction level applied initially was sufficient to keep the injected fluid in a small, well-defined region adjacent to the wall. In the next step, the level of suction was gradually reduced until hairpin vortices were first observed. The suction level at this point is marked by the circle symbols. Owing to hysteresis effects, this upper boundary, separating flow with and without hairpins, was not uniquely determined by the suction level. Thus, the transition from flow with hairpins to flow without, while increasing the suction level, was higher (square symbols) than that found by going in the opposite direction (circle symbols).

When the suction was further decreased below the level indicated by the circle symbols, the shedding of hairpin vortices persisted over a certain range. At the lower boundary of this range, a transition from shedding hairpins to a continuous jet of dye without any apparent hairpin structure was observed. The triangle and plus symbols in figure 7 correspond to the upper and lower limits, respectively, of this transition zone. In contrast to the hysteresis effects associated with the determination
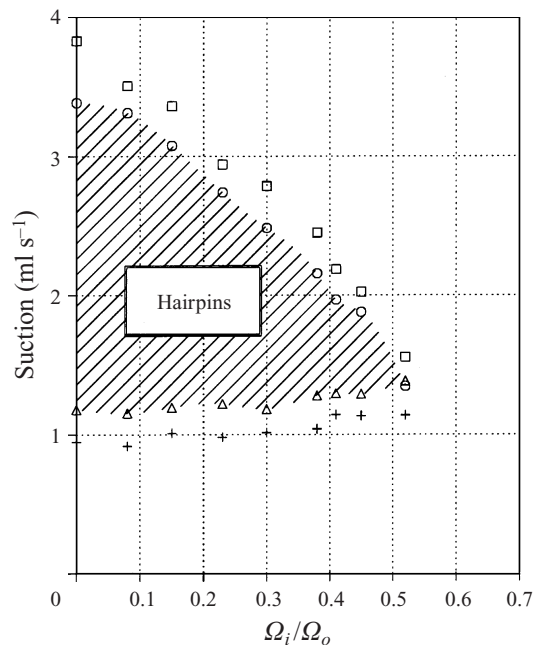
FIGURE 7. Domain of instability when $\Omega_o = 40$ r.p.m., described in terms of the suction level and the ratio Ω_i/Ω_o. The shaded area represents the range of parameters over which hairpin vortices could be clearly observed.

of the upper boundary of the instability domain, the boundaries of the transition zone, associated with the lower boundary of the instability domain, correspond to a suction level above which one can clearly distinguish the shedding of hairpins (upper limit), and below which, the flow of a continuous jet (lower limit). The shaded area in figure 7 represents the range of parameters over which hairpin vortices were always clearly distinguished and observed.

The upper boundary of the instability domain (the shaded area in figure 7) for the cases where $\Omega_o = 23$, 40 and 60 r.p.m. are shown in figure 8(*a*). The bottom boundary for each case is marked by the same symbol as that of the corresponding upper boundary, except that it contains the plus sign within it. It is seen that the bottom boundary is approximately a constant and does not depend on Ω_o. On the other hand, the upper boundary increases monotonically with Ω_o and thereby the region of instability is increased.

When the suction level associated with the upper boundary is made dimensionless, using the ratio between the average suction velocity, V_s (the suction flow rate divided by the area of the suction holes) and the azimuthal velocity of the outer cylinder ($V_o = \Omega_o R_o$), the data points of all three have approximately the same slope (figure 8*b*). Moreover, the data points corresponding to cases for which the outer angular velocity was greater than 20 r.p.m. follow the same curve shown by the solid line, which represents a least-squares fit to the data obtained with $\Omega_o = 40$ and 60 r.p.m. It should be noted that in figure 8(*b*), additional sets of data, corresponding to $\Omega_o = 30, 35, 50$ and 70 r.p.m., are included.

Inside the instability domain, hairpin vortices are shed periodically. The shedding frequency is plotted in figure 9 for the case in which $\Omega_o = 60$ r.p.m. The corresponding upper and lower boundaries of the instability region are shown respectively by the
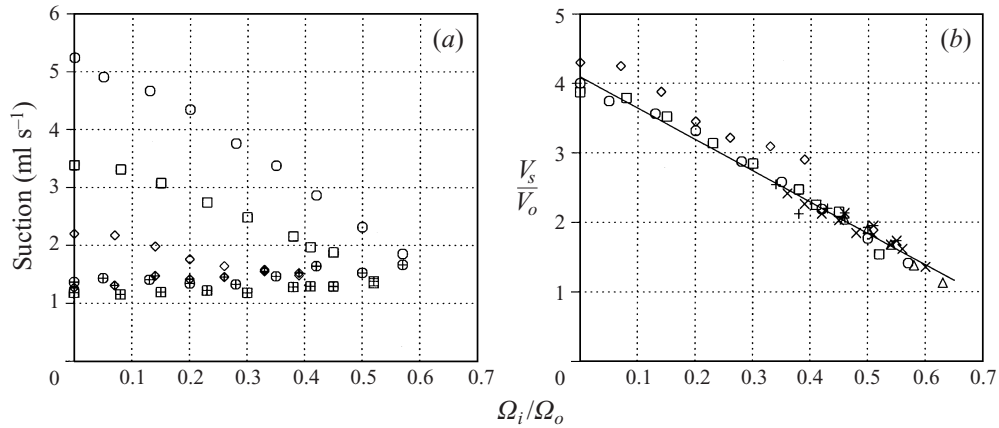
FIGURE 8. (a) Dimensional domains of instability. The diamonds, squares and circles mark the upper and lower (with the plus sign within) boundaries for $\Omega_o = 20$, 40 and 60 r.p.m., respectively. (b) The corresponding non-dimensional upper boundary of the instability domains. The star, plus, cross and triangle symbols correspond to $\Omega_o = 30$, 35, 50 and 70 r.p.m., respectively. The solid line is a least-squares fit to the data obtained with $\Omega_o = 40$ and 60 r.p.m.
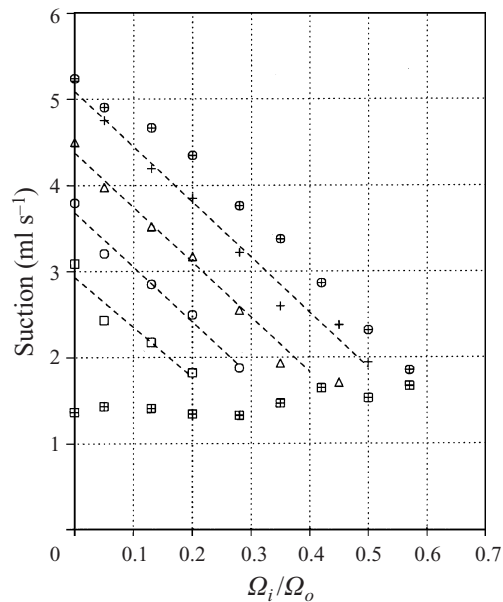

FIGURE 9. The shedding frequency of the hairpin vortices described in terms of the suction level and the ratio Ω_i/Ω_o; $\Omega_o = 60$ r.p.m. The upper and lower boundaries of the instability domain are indicated by the plus-marked circles and squares, respectively. Shedding frequency of $+$, 3 Hz; $\triangle$, 4 Hz; $\bigcirc$, 5 Hz; $\square$, 6 Hz. Dashed lines are fitted by least-squares error fit method.

plus-marked circles and squares. For a given ratio Ω_i/Ω_o, the suction level was varied between the upper and lower boundaries of the instability region. The shedding frequency was obtained by analysing a top-view flow visualization recording taken with a video camera that rotated with the inside cylinder. Each frequency value was calculated by timing the shedding of about 70 hairpins. For each value of Ω_i/Ω_o, the shedding frequency as a function of the suction level varied approximately linearly and

was curve fitted using the least-squares error fit method. This procedure was repeated for several values of Ω_i/Ω_o and shedding frequencies 3, 4, 5 and 6 Hz. As can be seen from the fitted linear dashed lines, the shedding frequency is approximately constant along lines which are nearly parallel to each other and to the upper boundary of the instability region. The frequency decreases towards the upper boundary (at which the shedding frequency approaches zero).

To summarize the results up to this stage, we first conclude that we found instability (growth of vortical structures away from the wall) in the range of parameters where the flow is known to be stable according to the Rayleigh criterion (14), but is unstable with respect to finite-amplitude localized disturbances as predicted by LC. Moreover, hairpin vortices could only be generated for sufficient levels of suction, which suggests that instability cannot occur for infinitesimal perturbations of the base flow. However, some of the experimental results found so far do not fully agree with the theoretical predictions. According to the results shown in figure 8(a), the right-most edge point of the instability domain depends on Ω_o and varies approximately from $\Omega_i/\Omega_o = 0.4$ for $\Omega_o = 23$ r.p.m. to $\Omega_i/\Omega_o = 0.6$ for $\Omega_o = 60$ r.p.m., whereas, for the given dimensions of R_i and R_o in our apparatus, the theoretical prediction for marginal stability (17), based on the axisymmetric Couette velocity profile (12), gives $\Omega_i/\Omega_o = 0.78$, independent of the angular velocity of the outer cylinder. In addition, the theoretical model applied to the axisymmetric Couette flow does not predict the existence of the upper limit of the instability domain found experimentally.

5.2. *The local mean flow*

In the following, we attempt to explain the difference between the values of marginal stability found in the experiments (the right-most edge point of the instability domain, see figures 7 and 8a) and the theoretical prediction based on the axisymmetric Couette velocity profile. As was mentioned in §2, the results of the theoretical model are general and only depend on the local flow field in the region of the disturbance. Therefore, we first examine the local mean flow in the region of the disturbance.

In figure 10, normalized azimuthal mean velocity profiles are plotted versus the azimuthal coordinate for two cases where $\Omega_o = 40$ r.p.m. The signals shown in figures 10a and 10b were measured when $\Omega_i/\Omega_o = 0.45$ and $\Omega_i/\Omega_o = 0.6$, respectively, corresponding to positions inside and outside the instability domain. The suction level was 1.47 ml s^{-1}. The velocity traces were measured at $z = 0$ and at 16 radial positions equally spaced between $r = 50.5$ (the lowest curve) and $r = 58$ mm (the top curve). The origin of the azimuthal coordinate is attached to the position of the suction holes. The deviation of the local mean flow from the undisturbed profiles (without suction) extends approximately from $-15°$ to $25°$. Relative to this range, the typical size of the observed hairpin is an order of magnitude smaller, about 1–2 mm, which corresponds approximately to $1°$–$2°$ in the azimuthal direction. Since the shedding of small hairpins is not correlated with the phase-locked procedure used to obtain these mean velocity measurements, there is no qualitative difference between the signals shown in figures 10(a) and 10(b).

The local mean flow between the two suction holes is characterized by an accelerated flow upstream of the holes and a decelerated flow near the holes, followed by an accelerated flow region further downstream. The observed hairpin vortices were measured between $\phi = 7.2°$ and $14.4°$. These boundaries are indicated by the two vertical dotted lines in each figure. The relatively uniform flow within this azimuthal interval, in particular about the centre of the hairpin at $r \approx 52.5$ mm, is indicative of the azimuthal interval being sufficiently far from the strong three-dimensional flow
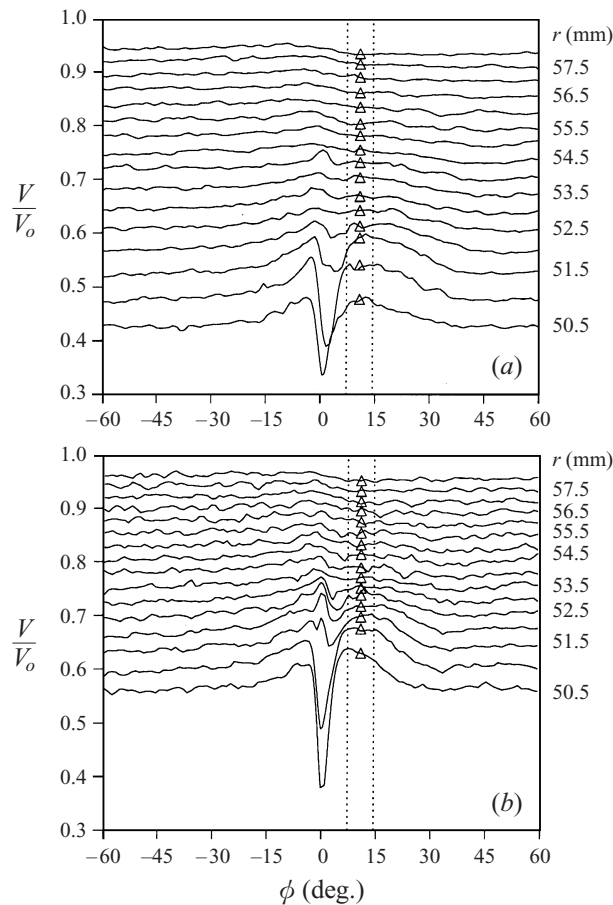
FIGURE 10. Normalized azimuthal mean velocity profiles, measured at $z = 0$ and at 16 radial positions, as function of the azimuthal coordinate. The suction level is 1.47 ml s^{-1}, $\Omega_o = 40$ r.p.m. and $\Omega_i/\Omega_o = 0.45$ (a) and 0.6 (b). The triangles represent an averaging value over the range $\phi = 7.2°$–$14.4°$.

at the suction holes (the region of generation), while the hairpin is still small. This allows us to make a comparison to local theory in this location as will be further discussed below. For most of the measurements and for a given radial position, the azimuthal velocity over the range $\phi = 7.2°$–$14.4°$ was averaged. The average velocities are indicated in figure 10 by the triangle symbols at $\phi = 10.8°$.

The azimuthal velocity profiles in the radial direction, measured for the case in which the suction level was 1.47 ml s^{-1}, $\Omega_o = 40$ r.p.m. and $\Omega_i/\Omega_o = 0.45$ are plotted in figure 11. The profiles, measured at $\phi = 10.8°, 25.2°$ and $180°$, are shown by the squares, diamonds and circles, respectively. Each point corresponds to an azimuthal average over $\pm 3.6°$. Also plotted in this figure is the velocity profile when no suction was applied (the plus-marked squares) and the theoretical Couette profile shown by the solid line.

As can be seen, the profile measured at $\phi = 180°$ is almost identical to the profile obtained when no suction was applied. As the azimuthal angle decreases, the deviation from this profile increases. From this figure, one can conclude that in the region of hairpin growth ($r \approx 52.5 \pm 1$ mm and $\phi \approx 10.8° \pm 3.6°$), the profiles subjected to
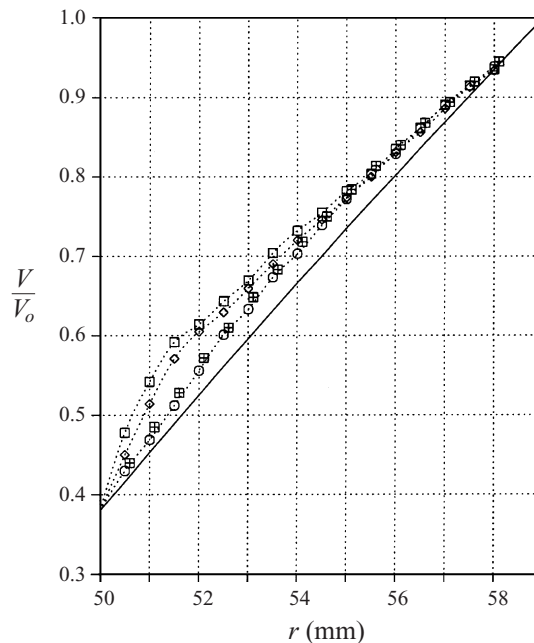
FIGURE 11. Radial distributions of the azimuthal velocity measured when the suction level was 1.47 ml s^{-1}, $\Omega_o = 40$ r.p.m., $\Omega_i/\Omega_o = 0.45$ and at □, $\phi = 10.8°$; ◇, $25.2°$; ○, $180°$. The plus-marked squares represent the velocity profile when no suction was applied and the theoretical Couette profile is shown by the solid line.

suction are significantly different from the profile measured when no suction was applied. Furthermore, this difference is larger when these profiles are compared with the Couette profile used in our preliminary theoretical prediction in §2. Because of this difference, in the following we shall use the local mean flow as an input to our model instead of the axisymmetric Couette flow. For this purpose, it is also important to note that the azimuthal variation of the local mean flow (the difference between the profiles measured at $\phi = 10.8°$ and $25.2°$) is relatively negligible when compared with the radial variation of the azimuthal velocity.

Finally, the variation of the local mean flow as a function of the azimuthal and axial coordinates for the case where $\Omega_o = 40$ r.p.m. and $\Omega_i/\Omega_o = 0.6$ is presented. In figure 12 a contour plot of $(V - V_{ns})/V_o$, the normalized difference between the local mean flow (V) subjected to suction (1.47 ml s^{-1}) and the local mean flow without suction (V_{ns}) at the same radial position ($r = 52.5$), is shown. The maximum difference occurs close to the position of the suction holes ($\phi = 0, z = \pm 3.5$ mm). As can be seen, the region enclosed between $z = \pm 3$ mm and $0 < \phi < 20°$, within which we observe the growth of the hairpin (the size of which is much smaller than the size of this region), is characterized by having approximately a constant azimuthal velocity. Moreover, within this region, the ratio $(dV/dz)/(dV/dr)$ is zero at $z = 0$ mm and has a maximum value of 0.03 at the boundaries ($z = \pm 4$ mm). Similar results were obtained for different conditions, i.e. different values of Ω_o and different values of Ω_i/Ω_o.

In summary, the local azimuthal mean velocity profiles measured in the region where the major growth of the hairpin takes place are significantly different from the theoretical solution (12). This difference may explain the lack of complete agreement
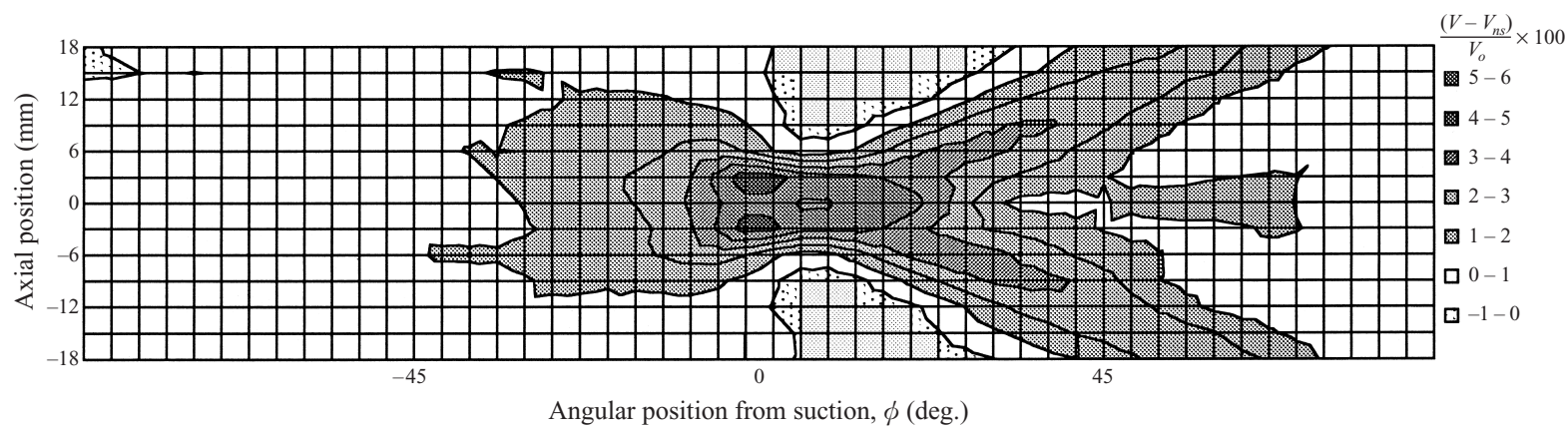
FIGURE 12. A contour plot of the normalized difference between the local mean azimuthal velocity subjected to suction ($1.47\,\mathrm{ml\,s^{-1}}$) and without suction measured at $r = 52.5\,\mathrm{mm}$, $\Omega_o = 40$ r.p.m. and $\Omega_i/\Omega_o = 0.6$.

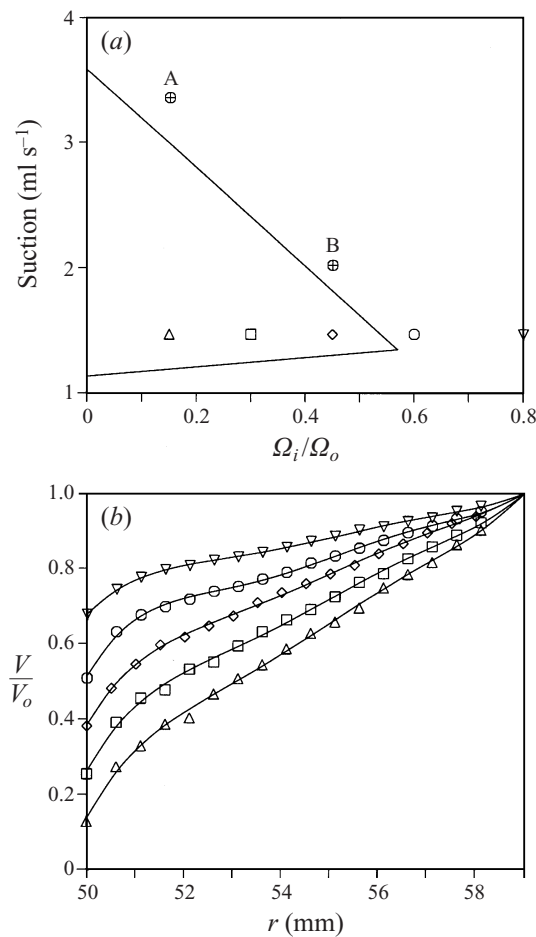E. Malkiel, V. Levinski and J. Cohen

FIGURE 13. (*a*) Positions of velocity profiles measurements with respect to a schematic drawing of the domain of instability at $\Omega_o = 40$ r.p.m. (*b*) Corresponding five azimuthal velocity profiles measured along a line of constant suction level (1.47 ml s^{-1}) at $\triangle$, $\Omega_i/\Omega_o = 0.15$; $\square$, $\Omega_i/\Omega_o = 0.3$; $\diamond$, $\Omega_i/\Omega_o = 0.45$; $\bigcirc$, $\Omega_i/\Omega_o = 0.6$; $\triangledown$, $\Omega_i/\Omega_o = 0.8$.

between the experimental results and the theoretical predictions, discussed at the end of §5.1. To check this possibility, the measured local azimuthal mean flow, which in accordance with the experimental results can be considered as a function of only the radial coordinate, will be used as an input to the theoretical model (see §2).

5.3. *The instability criterion based on local mean flow*

In this section, a comparison between the instability criterion based on local mean flow and the experimental results based on flow visualization is carried out. As was concluded in the previous section, the azimuthal local mean velocity is given by $V = V(r)$. The general instability criterion for this case is given by (7). As inferred from figure 11, the local mean profiles of the azimuthal velocity increase monotonically with the radial coordinate. Therefore, $[\mathrm{d}V/\mathrm{d}r + V/r]$ is always positive and the Rayleigh criterion for stability holds. In this case, for instability with respect

to finite-amplitude localized disturbances, we obtain

$$\left(\frac{\partial V}{\partial r} \bigg/ \frac{V}{r} \right) \bigg|_{r=r_d} > 3, \tag{23}$$

where r_d now corresponds to the radial position of the hairpin's centre.

To examine the local instability criterion (23) experimentally, several velocity profiles inside and outside the domain of instability were measured. The profiles plotted in figure 13(b) correspond to measurements carried out at $\Omega_o = 40$ r.p.m. along a line of constant suction level (1.47 ml s^{-1}) for five values of Ω_i/Ω_o, shown in figure 13(a). The level of suction was chosen to be close to the level corresponding to the right-hand edge point of the instability domain, delineated by the solid lines in figure 13(a). The points A and B correspond to measurements carried out when relatively high levels of suction were applied. Additional velocity profiles were also measured for several values of Ω_o. For each value of Ω_o, the velocity profiles were obtained under conditions determined by the suction level and the ratio Ω_i/Ω_o, so that their corresponding positions in relation to the boundaries of the domain of instability are approximately the same as in figure 13(a).

Based on fitted curves shown by the solid lines in figure 13(b), the radial distributions of $(dV/dr)/(V/r)$ are plotted in figure 14b using the same respective symbols. Similar profiles are also shown for the cases in which $\Omega_o = 23$ r.p.m. (figure 14a) and 60 r.p.m. (figure 14c). The vertical lines in these figures at $r = 52.5$ mm indicate the radial position of the hairpin's centre. The horizontal lines at $(dV/dr)/(V/r) = 3$ correspond to the marginal value for stability according to the local criterion. For example, in the case in which $\Omega_o = 60$ r.p.m., the first three profiles for $\Omega_i/\Omega_o = 0.1$, 0.3 and 0.5 are all above the horizontal line and therefore are unstable with respect to localized disturbances. The fourth curve, for which $\Omega_i/\Omega_o = 0.7$, is below the horizontal line for radial positions greater than 51.5 mm. Thus, in the latter case we expect stability. Similarly we find that for the case when $\Omega_o = 40$ r.p.m., the flow is unstable for $\Omega_i/\Omega_o \leqslant 0.45$ (diamonds, squares and upright triangles) and stable for $\Omega_i/\Omega_o \geqslant 0.6$ (circles and downturned triangles). These results are in full agreement with the experimental observations under the same conditions shown schematically in figure 13(a).

To formally determine the value of marginal stability for a given Ω_o, we use interpolation to obtain the ratio of Ω_i/Ω_o at which the curves of $(dV/dr)/(V/r)$ cross the horizontal line at the radial position of 52.5 mm. In figure 15, the theoretical predictions of marginal stability (hollow circles), based on the experimentally measured local basic velocity profiles, are compared with flow visualization results (the full circles). The latter results correspond to the locus of the right-most edge points of the instability domains presented in figure 8(a). Note that in figure 15 results obtained for three additional cases in which $\Omega_o = 30, 50$ and 70 r.p.m. are also included. The solid line represents a least-squares fit to the theoretically predicted values.

The agreement between the experimental observations and the predictions based on the local velocity profiles is fairly good. The difference between the two is about 20% for $\Omega_o = 23$ and 30 r.p.m., and is less than 10% for higher values of Ω_o. The accuracy in determining the marginal values based on flow visualization can be defined as the range of Ω_i/Ω_o between two limiting values. For values less than the lower limit, hairpins are always shed, while for values greater than the upper limit, hairpins are not observed. This accuracy is about 4% for $\Omega_o \geqslant 40$ r.p.m. and is decreased to about 15% for $\Omega_o = 23$ r.p.m.

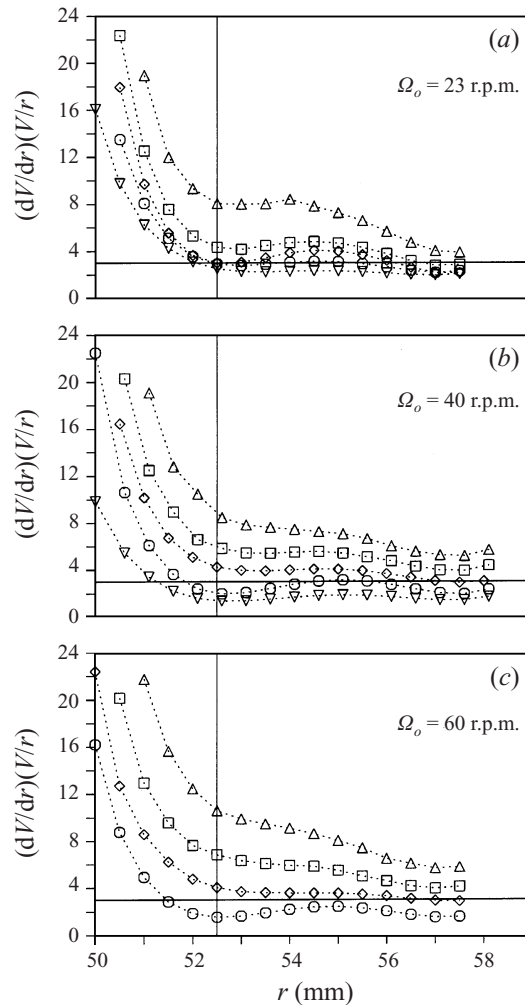It is more difficult to estimate the accuracy of the results based on local mean

FIGURE 14. Radial distributions of $(\mathrm{d}V/\mathrm{d}r)/(V/r)$ for (a) $\Omega_o = 23$ r.p.m. with suction of 1.47 ml s^{-1} at $\triangle$, $\Omega_i/\Omega_o = 0.16$; $\square$, $\Omega_i/\Omega_o = 0.35$; $\diamond$, $\Omega_i/\Omega_o = 0.45$; $\bigcirc$, $\Omega_i/\Omega_o = 0.54$; $\triangledown$, $\Omega_i/\Omega_o = 0.56$. (b) $\Omega_o = 40$ r.p.m. with suction of 1.47 ml s^{-1} at $\triangle$, $\Omega_i/\Omega_o = 0.15$; $\square$, $\Omega_i/\Omega_o = 0.3$; $\diamond$, $\Omega_i/\Omega_o = 0.45$; $\bigcirc$, $\Omega_i/\Omega_o = 0.6$; $\triangledown$, $\Omega_i/\Omega_o = 0.8$. (c) $\Omega_o = 60$ r.p.m. with suction of 1.71 ml s^{-1} at $\triangle$, $\Omega_i/\Omega_o = 0.1$; $\square$, $\Omega_i/\Omega_o = 0.3$; $\diamond$, $\Omega_i/\Omega_o = 0.5$; $\bigcirc$, $\Omega_i/\Omega_o = 0.7$.

velocity. There are several main sources for error in this case and not all of them can be accurately estimated. One source is the dependence of the criterion on the radial position of the hairpin. This error is approximately 4% over a radial distance of 1 mm. Another source is in the interpolation between curves of $(\mathrm{d}V/\mathrm{d}r)/(V/r)$ above and below the criterion. This error depends on the closeness of the profiles in the vicinity of $r = 52.5$ mm to the marginal value of 3. For example, for the case of $\Omega_o = 40$ r.p.m., the error in interpolation is estimated by taking the interpolation between the corresponding values obtained at $\Omega_i/\Omega_o = 0.45$ and 0.8 (or between $\Omega_i/\Omega_o = 0.3$ and 0.6) instead of the interpolation carried out between the corresponding values associated with $\Omega_i/\Omega_o = 0.45$ and 0.6. Using this procedure for the entire sets of data the average error due to the interpolation was estimated to be about 5%. It should be noted that for clarity, not all of the available sets of the data are shown in figure 14.
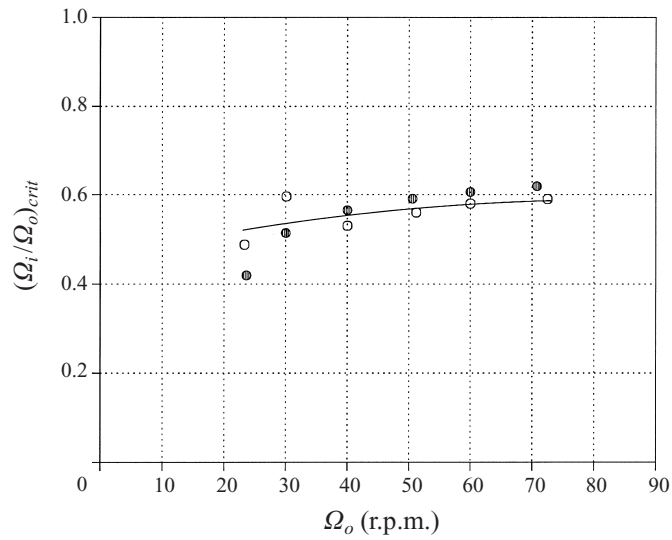
FIGURE 15. Comparison of the criterion for marginal stability between the theoretical predictions (hollow circles) and flow visualization results (the shaded circles). The solid line represents a least-squares fit to the theoretically predicted values.
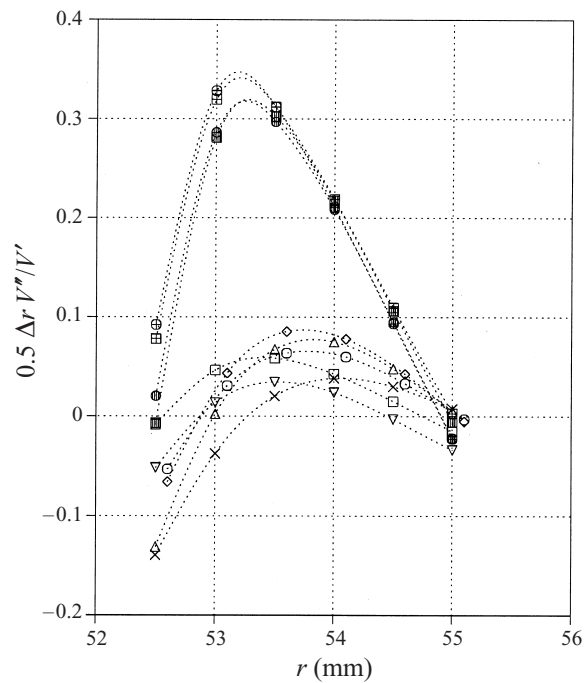

FIGURE 16. Radial distributions of the ratio $0.5\Delta r V''/V'$ for $\Omega_o = 40$ r.p.m. with suction of 1.47 ml s^{-1} at $\bigcirc$, $\Omega_i/\Omega_o = 0.15$; $\diamond$, $\Omega_i/\Omega_o = 0.3$; $\triangle$, $\Omega_i/\Omega_o = 0.45$; $\oplus$, with suction of 3.36 ml s^{-1} at $\Omega_i/\Omega_o = 0.15$; $\bullet$, with suction of 2.02 ml s^{-1} at $\Omega_i/\Omega_o = 0.45$. $\Omega_o = 60$ r.p.m. with suction of 1.71 ml s^{-1} at $\square$, $\Omega_i/\Omega_o = 0.1$; $\triangledown$, $\Omega_i/\Omega_o = 0.3$; $\times$, $\Omega_i/\Omega_o = 0.5$; $\boxplus$, with suction of 4.96 ml s^{-1} at $\Omega_i/\Omega_o = 0.15$; $\blacksquare$, with suction of 2.90 ml s^{-1} at $\Omega_i/\Omega_o = 0.45$.

In addition to the experimental errors mentioned above, there is another group of possible errors associated with the difference between the experimental conditions and the theoretical assumptions. The first source for such an error is related to the assumption that the mean velocity field includes only the azimuthal component and the latter is a function of the radial coordinate only. Using the measured local mean velocity field, the maximum of the ratios $(\partial V/\partial z)/(\partial V/\partial r)$ and $(\partial V/r\partial\phi)/(\partial V/\partial r)$ are estimated to be 0.025 and 0.05, respectively. Thus, the error due to this theoretical assumption is not significant.

The second source of error associated with the inconsistency between the theoretical assumptions and the experimental conditions is related to the theoretical approximation of the mean velocity profile in the region of the disturbance being given by Taylor series expansion only up to the leading term (LC). For this approximation to be valid, the ratio $0.5\Delta r V''/V'$, where Δr is the radius of a sphere enclosing the hairpin, must be small. Typical radial distributions of this ratio are plotted in figure 16. According to experimental observations, the value of Δr is about 1.5 mm. The plus marked and full circles correspond to measurements obtained at points A and B in figure 13(a), respectively, when $\Omega_o = 40$ r.p.m. Similar measurements, obtained at respective points for the case when $\Omega_o = 60$ r.p.m., are shown by the plus-marked and filled squares. The hollow and cross symbols correspond to values obtained along the constant low suction levels within the domains of instability (see figure 13a) for the cases in which $\Omega_o = 40$ and 60 r.p.m.

While for the low-suction cases the error due to the theoretical approximation of the local mean velocity is about 10%, the error is much more significant for the high-suction cases. As can be seen from figure 16, the radial distribution of $0.5\Delta r V''/V'$ at points along the upper boundary of the instability domain is almost the same (for both cases of Ω_o) and has a maximum value of 0.35, which cannot be considered small as assumed in the theory (LC). This may explain why, at relatively high levels of suction, the flow becomes stable with respect to localized disturbances at values of Ω_i/Ω_o smaller than the predicted value for stability based on the local mean flow.

In summary, the experimental observations of the largest values of Ω_i/Ω_o beyond which the flow is stable with respect to finite-amplitude localized disturbances are well predicted by the theory based on the local mean flow. The difference between the two is within the expected accuracy which is about 10% for $\Omega_o \geqslant 40$ r.p.m. and about 20% for lower values of Ω_o.

5.4. *The inclination angle of the hairpin*

In this section, a comparison of the inclination angle of the hairpin between the theoretical prediction based on local mean flow and the experimental results based on flow visualization is carried out. Using the results of §2 and substituting (9) into (11), the inclination angle Θ between the plane of the vortex and the radial direction is

$$\Theta = \arctan\left(\left(\frac{\partial V}{\partial r} - 3\frac{V}{r}\right)\Big|_{r=r_d} \Big/ \left(\frac{\partial V}{\partial r} + \frac{V}{r}\right)\Big|_{r=r_d}\right)^{1/2}, \qquad (24)$$

where the radial position of the hairpin's centre is $r_d = 52.5$ mm.

The theoretical evaluation of Θ is made in a similar way to the method described in the previous section. In other words, for various flow conditions we use curves fitted to the measured local mean velocity profiles to obtain the velocity and its first derivative at r_d.

The experimental inclination angles were determined from top-view images of
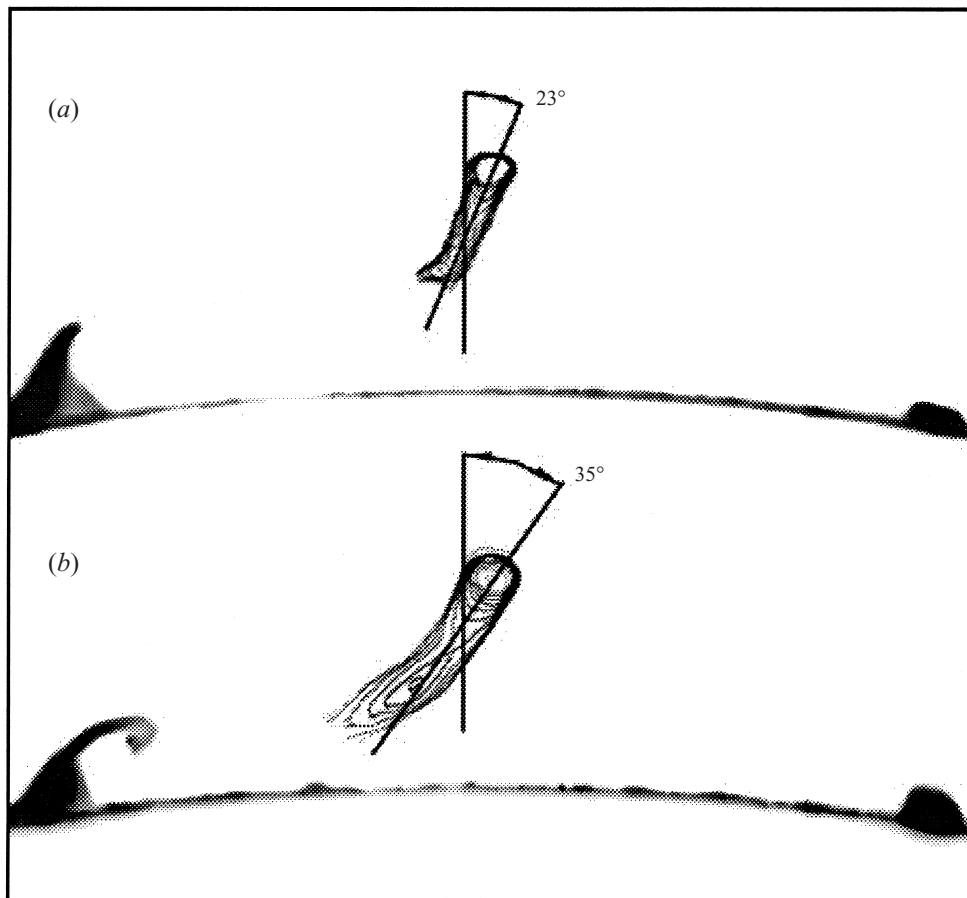
FIGURE 17. Inclination angles measured at $r = 52.5$ mm between the radial direction (the vertical line) and a line along the axis of the vortex core. The suction level is 1.85 ml s^{-1} and $\Omega_o = 60$ r.p.m. (a) $\Omega_i/\Omega_o = 0.5$, (b) $\Omega_i/\Omega_o = 0$.

hairpins after image enhancement and processing. In order to reduce the amount of scatter in the resulting data, only symmetric hairpins were selected for measurement. This was achieved by using simultaneously captured side views and by selecting hairpins based on leg symmetry and position in relation to the centreline plane between the suction holes (using the 15° mark).

Top views of hairpin vortices obtained for a fixed value of $\Omega_o = 60$ r.p.m. and two angular velocity ratios of $\Omega_i/\Omega_o = 0.5$ and 0, with the suction level at 1.85 ml s^{-1}, are shown in figures 17(a) and 17(b), respectively. These images were output from an edge-finding algorithm that was applied to the raw image files. The outer surface of the inner cylinder is indicated by the black arcs at the bottom of each figure. The spots on the left and right edges of each arc correspond to the position of the suction holes ($\phi = 0$) and a position on the inner cylinder where $\phi = 15°$, respectively. The inclination angles are measured between the radial direction (the vertical line) and a line along the axis of the vortex core in a region close to the vortex head. The two lines cross at $r = 52.5$ mm. As was pointed out by Haidari & Smith (1994) and can also be deduced from figure 4, the evaluation of the inclination angle based on flow visualization is somewhat arbitrary owing to the curvature of the hairpin.
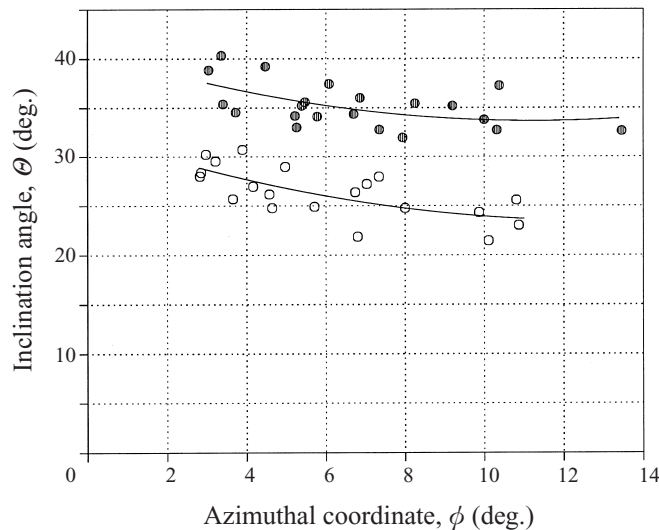
FIGURE 18. Azimuthal variation of the inclination angle. The suction level is $1.85 \, \mathrm{ml \, s^{-1}}$, $r = 52.5 \, \mathrm{mm}$ and $\Omega_o = 60$ r.p.m. The hollow and filled circles represent measurements obtained when $\Omega_i/\Omega_o = 0.5$ and 0, respectively.

Nevertheless, we use the above definition for the inclination angle since it is the most appropriate for the comparison with the theoretically predicted value (24). The latter, in accordance with the integral character of the fluid impulse (1), represents the average value of the growing part of the hairpin.

As can be seen from figure 17, the angle is decreased significantly when the angular velocity of the inner cylinder is increased, as is predicted by the theory (24). The respective theoretical values for the cases shown in figures 17(a) and 17(b) are 25° and 41°. Thus, the measured inclination angles are within 15% of the predicted values.

A set of inclination angles measured within an azimuthal range between $\phi = 3°$ and 14°, and obtained under the same conditions as those corresponding to figure 17, is shown in figure 18. The hollow and full circles represent measurements obtained when the angular velocity ratios were $\Omega_i/\Omega_o = 0.5$ and 0, respectively. The measured angles were curve fitted (the solid lines) using the least-squares error fit method. As can be seen, the inclination angle decreases slightly as the azimuthal coordinate is increased. The fitted curve for the angles measured when $\Omega_i/\Omega_o = 0.5$ is within $\pm 10\%$ of the predicted value (25°). The fitted curve for the angles measured when the inner cylinder was stationary is always lower (10–20%) than the predicted angle (41°). The scattering of the data (about 10%) is probably due to the influence of the residual vorticity resulting from the periodicity of the annular domain.

6. Summary and discussion

In this paper, the predictions of a recent theoretical model (LC) describing the instability of shear flows with respect to finite-amplitude localized disturbances was examined experimentally.

Before proceeding with the summary of the results, we would like to clarify the term 'stability' used in conjunction with the theoretical model (LC). According to the theory, the term stability (instability) means that the fluid impulse of a closed

vortical disturbance, localized in all three directions, will not grow (or grow) in time. The above stability definition is not equivalent to the conventional criteria of linear and energy stability. In fact, the growth of the fluid impulse does not necessarily guarantee growth in energy of the localized disturbance or vice versa. For example, viscous diffusion leads to the decay of the localized disturbance energy while its fluid impulse remains the same. On the other hand, the geometrical stretching of a closed vortex loop while its circulation remains unchanged will result in the growth of its fluid impulse, indicating instability according to the above definition. Although this definition, which associates the geometrical growth of localized vortical structures with instability, cannot describe the evolution of 'wavy' disturbances or 'quasi' two-dimensional structures for which the fluid impulse integral is not defined, it is very suitable for describing the growth of hairpin vortices in shear flows.

According to the theoretical model, planar unidirectional flows are always unstable with respect to finite-amplitude localized disturbances. For this reason, in this paper we focused on an axisymmetric rotating shear flow for which a stability criterion is predicted to exist. In addition, unlike plane shear flows in which the inclination angle of the growing vortex is predicted to be $45°$ (LC), this angle in the case of rotating shear flows is found theoretically to be a function of the base flow parameters.

A series of experiments was conducted in an axisymmetric Couette apparatus in the range of parameters (R_o, R_i, Ω_o and Ω_i) where the flow is known to be linearly stable, but may be unstable with respect to localized disturbances as predicted by LC. Hairpin vortices, similar to the ones reported for the case of a laminar boundary layer (e.g. Acarlar & Smith 1987a, b), were observed (see figure 4). The associated instantaneous velocity field (see figure 5) resembles the bursting phenomenon observed in turbulent boundary layers and was shown to be a superposition of the unperturbed flow and the flow induced by the hairpin.

For a quantitative comparison between the experimental observations and the theoretical predictions, the local mean flow in the region within which the growth of hairpins was observed had to be used as an input to the theoretical model instead of the axisymmetric Couette flow. Indeed, the theoretical predictions concerning the marginal value for instability (the highest value of Ω_i/Ω_o beyond which the flow is stable), based on the measured local mean velocity profiles, are in good agreement with the experimental observations. In addition, measurements of the inclination angles of hairpin vortices under various external flow conditions show good qualitative agreement with the theoretical predictions.

For values of Ω_i/Ω_o smaller than the marginal value for stability (predicted by the theory) and depending on the level of suction applied, a domain of instability bounded by upper and lower boundaries (see figure 7) was found. In our experiments, the initial vortex disturbance was generated by applying a controlled amount of suction which caused the formation of a locally separated region attached to the inner cylinder. Hairpin vortices were observed to grow and move away from the wall only for sufficient levels of suction (the bottom boundary of the instability domain). In that respect, the existence of this boundary suggests the need for a minimal size of the separated region in order for hairpins to shed. This minimal size can be related to a minimal amplitude of the initial disturbance which can be estimated as the difference in velocities with and without suction at the edge of the separated flow, i.e. $h\mathrm{d}V/\mathrm{d}r$, where h is the height of the separated region. Thus, on one hand the experimental results do not contradict the prediction (of stability) of the linear theory and on the other hand they support the prediction (of instability) of the theoretical model (LC) for which the amplitude of the disturbance does not have to be infinitesimally small.

In this respect, the instability mechanism described here can also be related to the transition process of flows dominated by the rotation of the outer cylinder, which as was observed by Coles (1965) occurred only when sufficiently strong disturbances were present.

The slope of the upper boundary was found to be parallel to the slope of lines along which the shedding frequency of the hairpins is constant. The value of the shedding frequency is decreased towards the upper boundary, which can be considered as the line along which the frequency is zero. Along the upper boundary, the radial distribution of the ratio $0.5\Delta r V''/V'$ was found to be self-similar, having a maximum value of about 0.35. This contradicts the assumption used in the theory that the disturbance is localized such that the mean velocity field in its region can be described by the leading term of its Taylor series expansion. This is probably the reason why the existence of the upper boundary is not predicted by the theoretical model (LC).

Based on the experimental results, we conclude that the theoretical criterion (23) is sufficient in predicting stability. In other words, the theory is capable of determining the conditions under which the initial vortex disturbance will not grow. This supports our explanation of the evolution of localized disturbances in shear flows. As was shown by LC, the theoretical model describes a simple feedback mechanism for the growth of localized vortical disturbances in shear flows (see §1). The model is general in the sense that it can be applied to any three-dimensional base flow provided the disturbance is localized and all dimensions thereof are much smaller than a dimensional length scale corresponding to an $O(1)$ change of the external (unperturbed) velocity.

However, the experimental results show that the model provides only a necessary condition for instability. Thus, for instability to occur, more conditions associated with the initiation of the vortical disturbance need to be satisfied. These conditions (which are outside the scope of the present paper) are related to the local mean flow in the region of the disturbance. In our case the local mean flow was determined by the amount of suction applied. In laminar boundary layers, the triggering mechanism for the initiation of hairpins was an artificial protuberance or fluid injection (Acarlar & Smith 1987*a, b*) or a finite-amplitude acoustic excitation leading to subcritical transition (Masahito & Nishioka 1995). In natural turbulent boundary layers, the lift-up of low-speed streaks is believed to precede the bursting events (Kline *et al.* 1967; Landahl 1975).

REFERENCES

ACARLAR, M. S. & SMITH, C. R. 1987*a* A study of hairpin vortices in a laminar boundary layer. Part 1. Hairpin vortices generated by a hemisphere protuberance. *J. Fluid Mech.* **175**, 1.

ACARLAR, M. S. & SMITH, C. R. 1987*b* A study of hairpin vortices in a laminar boundary layer. Part 2. Hairpin vortices generated by fluid injection. *J. Fluid Mech.* **175**, 43.

BATCHELOR, G. K. 1967 *An Introduction to Fluid Dynamics*, pp. 517–520. Cambridge University Press.

COLES, D. 1965 Transition in circular Couette flow. *J. Fluid Mech.* **21**, 385.

ESCUDIER, M. P., GOULDSON, I. W. & JONES, D. M. 1996 Circular Couette flow and Taylor vortices in shear-thinning liquids. In *Developments in Laser Techniques and Applications to Fluid Mechanics: Proc. 7th Intl. Symp, Lisbon, Portugal, 11–14 July, 1994*, pp. 16–33. Springer.

HAIDARI, A. H. & SMITH, C. R. 1994 The generation and regeneration of single hairpin vortices. *J. Fluid Mech.* **227**, 135.

HEAD, M. R & BANDYOPADHYAY, P. 1981 New aspect of turbulent boundary-layers structure. *J. Fluid Mech.* **107**, 297.

KAFTORI, D., HETSRONI, G. & BANERJEE, S. 1994 Funnel-shaped vortical structures in wall turbulence. *Phys. Fluids* **6**, 3035.

KLINE, S. J., REYNOLDS, W. C., SCHROUB, F. A. & RUNSTADLER, P. W. 1967 The structure of turbulent boundary layers. *J. Fluid Mech.* **30**, 741.

KOSCHMIEDER, E. L. 1993 *Benard Cells and Taylor Vortices*. Cambridge University Press.

LANDAHL, L. 1975 Wave breakdown and turbulence. *SIAM J. Appl. Maths* **28**, 775.

LEVINSKI, V. & COHEN, J. 1995 The evolution of a localized vortex disturbance in external shear flows. Part 1. Theoretical considerations and preliminary experimental results. *J. Fluid Mech.* **289**, 159.

MASAHITO, A. & NISHIOKA, M. 1995 Boundary-layer transition triggered by hairpin eddies at subcritical Reynolds numbers. *J. Fluid Mech.* **297**, 101.

ROBINSON, S. K. 1991 Coherent motions in the turbulent boundary layer. *Ann. Rev. Fluid Mech.* **23**, 601.

SMITH, C. R. & WALKER, J. D. A. 1995 Turbulent wall-layer vortices. In *Fluid Vortices* (ed. S. I. Green), pp. 235–290. Kluwer.

THEODORSEN, T. 1952 Mechanism of turbulence. *Proc. 2nd Midwestern Conf. on Fluid Mech.* Ohio state University.